Meteoritics & Planetary Science 36, 1225–1236 (2001)
Available online at http://www.uark.edu/meteor

Radar observations of asteroid 1998 ML14

STEVEN J. OSTRO[1]*, R. SCOTT HUDSON[2], LANCE A. M. BENNER[1], MICHAEL C. NOLAN[3], JON D. GIORGINI[1], DANIEL J. SCHEERES[4], RAYMOND F. JURGENS[1] AND RANDY ROSE[1]

[1]Jet Propulsion Laboratory, California Institute of Technology, Pasadena, California 91109-8099, USA
[2]School of Electrical Engineering and Computer Science, Washington State University, Pullman, Washington 99164-2752, USA
[3]Arecibo Observatory, HC3 Box 53995, Arecibo, Puerto Rico 00612, USA
[4]Department of Aerospace Engineering, University of Michigan, Ann Arbor, Michigan 48109-2140, USA
*Correspondence author's e-mail address: ostro@reason.jpl.nasa.gov

(Received 2001 April 17; accepted in revised form 2001 May 24)

Abstract–Goldstone and Arecibo delay-Doppler radar imaging of asteroid 1998 ML14 shortly after its discovery reveals a 1 km diameter spheroid with prominent topography on one side and subdued topography on the other. The object's radar and optical properties are typical for S-class near-Earth asteroids. The gravitational slopes of a shape model derived from the images and assumed to have a uniform density are shallow, exceeding 30° over only 4% of the surface. If 1998 ML14's density distribution is uniform, then its orbital environment is similar to a planetary body with a spheroidal gravitational field and is relatively stable. Integration of a radar-refined orbit reveals that the 1998 apparition was the asteroid's closest approach to Earth since at least 1100 and until 2283, when it approaches to within 2.4 lunar distances. Outside of that time interval, orbit uncertainties based on the present set of observations preclude reliable prediction.

INTRODUCTION AND OVERVIEW OF THE OBSERVATIONS

1998 ML14 was discovered in late June 1998 by LINEAR (M.P.E.C. 1998-M26) at White Sands, New Mexico. A Mars-crosser with a semimajor axis of 2.42 AU and a perihelion distance of 0.926 AU, it is currently in a 4:15 orbital-period resonance with Earth and a 1:2 resonance with Mars. The asteroid's trajectory brought it within 0.018 AU (seven lunar distances) from Earth on 1998 August 11 at declination = –44°, and then northward into the declination windows of Goldstone (declinations greater than –30°) on August 13 and Arecibo (declinations within 19.7° of 18.3°) on August 15. Estimates of echo strengths based on initial estimates of the asteroid's absolute visual magnitude ($H \approx 17.5$, corresponding to a diameter of about a kilometer) predicted an excellent imaging opportunity (Table 1), and target-of-opportunity telescope time was requested at each radar facility.

In early July, the pointing uncertainty ($\Delta\theta$) for the mid-August opening of the radar window was 12°, much larger than the two-arcminute radar beam widths. Follow-up astrometry shrunk $\Delta\theta$ to a few degrees by July 5. After a two-week gap, astrometric measurements resumed, shrinking $\Delta\theta$ to 0.3° by July 24, an arcminute by August 3, and 2 arcseconds by August 11. Most of the critical July astrometry was obtained by G. Garradd at Loomberah, Australia, and by S. McAndrew at North Ryde, Australia. The first Goldstone observations, on August 13–14, shrunk $\Delta\theta$ below the arcsecond level and reduced uncertainties in predictions of Doppler frequency and time delay from ~200 Hz and 8000 μs to 0.5 Hz and 60 μs.

On August 7, Hicks and Weissman (pers. comm.; see also Hicks and Weissman, 1998) reported observations at Las Campanas Observatory during July 12–14: "The R-band photometry yields a double peaked lightcurve of modest amplitude of 0.12 mag and a period of 14.98 ± 0.06 h and a mean absolute magnitude in the R-band of 16.94 (assuming $G = 0.25$). The solar subtracted colors for this object are most compatible with an S-type asteroid." Advance knowledge of the asteroid's spin period greatly simplified the radar observations.

Our strategy at Goldstone was to refine the delay-Doppler prediction ephemerides enough to ensure that images would not be smeared, and to do imaging with enough rotation-phase coverage to allow preliminary estimation of the object's shape. Then the greater sensitivity of the upgraded Arecibo Observatory could be exploited to obtain higher quality images and to refine the shape model. The Arecibo radar had returned to operation in the spring, and this experiment coincided with initial use of its new delay-Doppler imaging system.

Almost all the observations proceeded as planned. Table 2 gives setups and start/stop times for useful runs at each observatory. All delay/Doppler/pointing ephemerides were generated using JPL's on-site orbit determination (OSOD)

Prelude preprint MS#4528

© Meteoritical Society, 2001. Printed in USA.

TABLE 1. Ephemeris and predictions of signal-to-noise ratio (SNR).

Date	RA	Declination	Distance (AU)	GOLDSTONE Date SNR	GOLDSTONE Run SNR	ARECIBO Date SNR	ARECIBO Run SNR
1998 August 13	75°	−17°	0.022	1900	140	0	0
1998 August 14	85°	−2°	0.029	1300	65	0	0
1998 August 15	88°	4°	0.034	650	36	8000	1300
1998 August 16	91°	8°	0.040	260	20	5600	760
1998 August 17	93°	11°	0.046	150	11	3500	500
1998 August 18	95°	14°	0.052	90	7	2100	300

These SNR predictions assume asteroid diameter = 1.0 km, as implied by the object's absolute magnitude $H = 17.5$ (M.P.E.C. 1998-M26) and its S classification; rotation period = 15 h; and optimum radar system parameters anticipated for Goldstone (transmitter power = 150 kW, system temperature = 18 K, antenna gain = 74 dB, sensitivity = 0.9 K/Jy) and Arecibo (transmitter power = 900 kW, system temperature = 30 K, antenna gain = 72 db, sensitivity = 7.3 K/Jy).

program. Improved orbit solutions incorporating new radar astrometry were generated at several stages of the experiment, as indicated in Table 2. Figure 1 sketches the phase coverage for the Doppler-only (cw) runs, the coarse-resolution delay-Doppler runs (used just for refining ephemerides), and the high-resolution delay-Doppler imaging runs. Descriptions of our observation and data-reduction techniques as well as relevant radar astronomical terminology are available in Ostro *et al.* (1999) and are not repeated here.

RADAR ASTROMETRY AND ORBIT REFINEMENT

Table 3 lists our useful radar astrometric measurements and Table 4 gives estimates of 1998 ML14's orbital elements

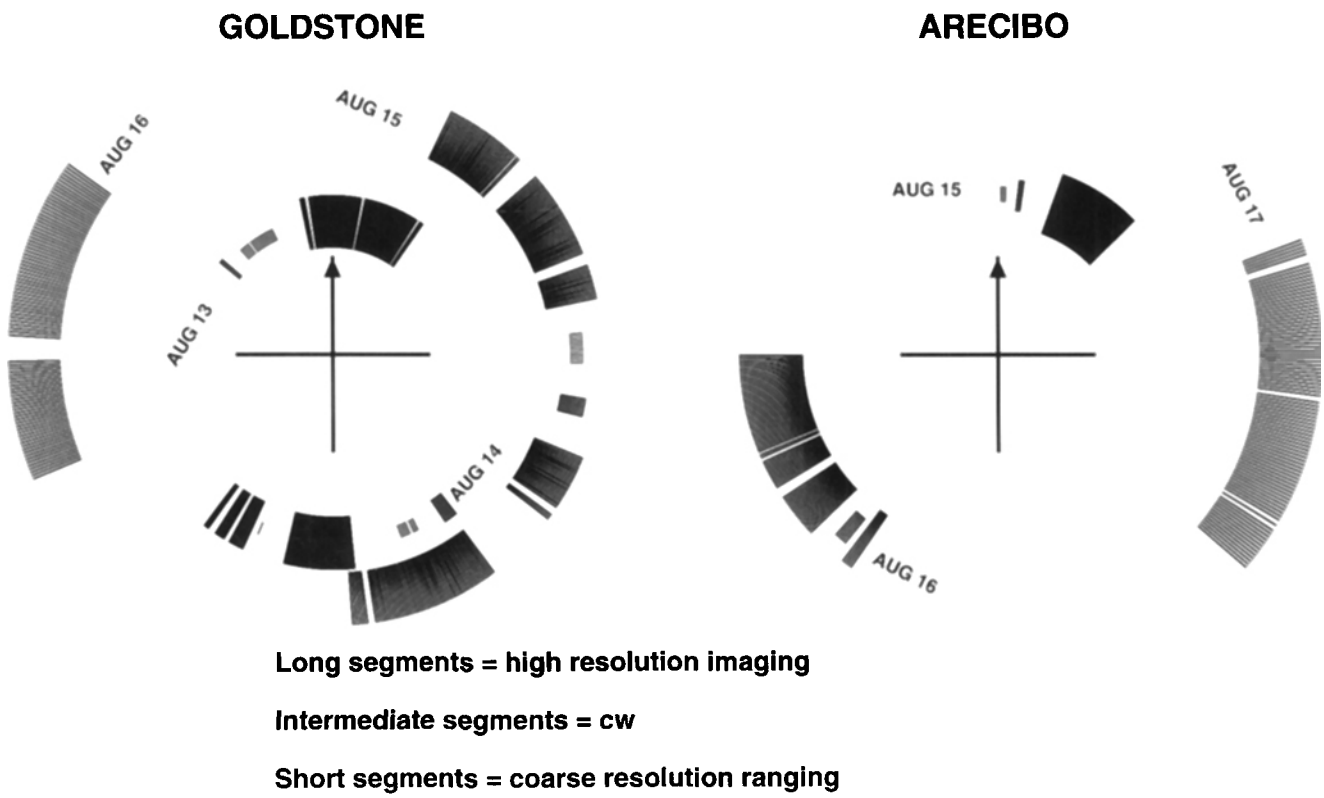

FIG. 1. Rotation phase coverage. Each radial line segment indicates the phase of a single run, and each ring corresponds to echoes obtained on a different date, where the first day at each observatory is indicated with the innermost ring and the last with the outermost ring. The zero-phase epoch is 1998 August 13.0 and phase increases clockwise. Long, intermediate, and short segments correspond respectively to high-resolution imaging, cw, and coarse-resolution ranging.

TABLE 2. Experiment masterlog.

File	Resolution		Offsets	Code	FFT	OSOD	Runs	Start-stop	PTX
	Time (μs)	Frequency (Hz)							
GOLDSTONE August 13 (DOY 225)									
98225A	cw	0.24	none	none	4096	29	6	125131-125614	150
22503	10	6	none	127	64	29	11	131518-132520	150
22504	11	6	none	127	64	29	29	132825-135430	150
22507	0.125	0.5	6 Hz	127	64	31	5	142928-143334	150
22508	0.125	0.5	10 Hz	127	64	31	50	143736-152546	150
22509	0.125	0.5	10 Hz	127	64	31	53	152908-161947	150
22510	0.125	0.5	10 Hz	127	64	31	4	162250-162610	150
GOLDSTONE August 14 (DOY 226)									
98226	cw	0.24	none	none	4096	33	10	115301-120249	150
22603	7	4	none	127	64	33	4	122234-122627	150
22604	10	6	none	127	64	33	7	122904-123613	150
22607	0.125	0.5	10 Hz	127	64	35	44	131255-140104	150
22610	0.125	4	10 Hz	127	64	35	1	142410-142439	150
22611	0.125	0.5	10 Hz	127	64	35	9	142958-143858	150
22612	0.125	0.5	10 Hz	127	64	35	7	144412-145107	150
22613	0.125	0.5	10 Hz	127	64	35	4	145644-150019	150
GOLDSTONE August 15 (DOY 227)									
22703	0.125	0.5	10 Hz	127	64	37	34	130106-134514	140
22704	0.125	0.5	10 Hz	127	64	37	38	135734-144121	140
22705	0.125	0.5	10 Hz	127	64	37	15	145202-151026	140
22706	7	4	none	127	64	37	15	152748 154640	140
98227	cw	0.24	none	none	4096	37	10	160444-161610	140
22707	0.125	0.5	10 Hz	127	64	39	24	163610-170613	140
22708	0.125	0.5	6 Hz, 3.75 μs	127	64	39	3	171032-171342	140
22709	0.125	0.5	6 Hz, 3.75 μs	127	64	39	54	175332-190238	140
22710	0.125	0.5	6 Hz, 3.75 μs	127	64	39	7	190636-191500	140
GOLDSTONE August 16 (DOY 228)									
22804	0.125	0.5	6 Hz	127	64	39	36	131209-140230	150
22805	0.125	0.5	6 Hz	127	64	39	52	141628-153750	150
ARECIBO August 15 (DOY 227)									
ml15u4	4	0.12	10 Hz	4095	512	37	5	115735-120355	970
cw	cw	0.08	10 Hz	none	65536	37	5	121240-121845	940
ml15up3**	0.3	0.10	10 Hz	16383	2048	37	53	124450-135055	900
ARECIBO August 16 (DOY 228)									
ml16up2*	0.2	0.07	10 Hz	16383	4096	39	5	115000-115701	780
cw	cw	0.08	10 Hz	none	65536	39	7	120100-121053	770
ml16up2*	0.2	0.07	10 Hz	16383	4096	39	18	121920-124459	780
ml16up3**	0.3	0.10	10 Hz	16383	2048	39	53	125030-140815	890
ARECIBO August 17 (DOY 229)									
ml17up3**	0.3	0.10	10 Hz	16383	2048	39	5	114410-115219	810
ml17up2*	0.2	0.07	10 Hz	65535	1024	39	83	115520-141649	780

Useful data files obtained at Goldstone and Arecibo are listed chronologically for each site along with their time/frequency resolutions. DOY is day of year and times are U.T.C. Data records were written using 12-bit words unless otherwise indicated. Sometimes offsets were inserted to more conveniently position echoes in the data's delay/Doppler window. Time-resolved setups used a repetitive, binary-phase-coded waveform with the indicated code length. FFT is the length of the Fast Fourier Transform used. The column labeled OSOD identifies the orbit solution used for the observing ephemerides. A "run" is a transmit-receive cycle. PTX is transmitter power in kilowatts.

*Data records clipped to one-bit words.

**Data records clipped to two-bit words.

TABLE 3. 1998 ML14 radar astrometry.

U.T.C. epoch of echo reception	Obs.	Time delay or Doppler frequency estimate and uncertainty			OSOD-55 residual
1998 August 13 12:50:00	G	−441334.2 Hz	±	2.0 Hz	1.47 Hz
1998 August 13 13:30:00	G	25.0319135 s	±	20.0 μs	8.90 μs
1998 August 13 15:10:00	G	−461352. Hz	±	2.0 Hz	1.67 Hz
1998 August 14 11:50:00	G	−506955.2 Hz	±	1.5 Hz	−0.04 Hz
1998 August 14 12:30:00	G	29.8648855 s	±	10.0 μs	−2.61 μs
1998 August 14 13:40:00	G	−517701.3 Hz	±	1.5 Hz	0.16 Hz
1998 August 14 13:40:00	G	30.11855135 s	±	2.0 μs	−0.22 μs
1998 August 15 13:00:00	G	−555035.7 Hz	±	1.5 Hz	0.57 Hz
1998 August 15 13:00:00	G	35.572954 s	±	2.0 μs	−0.65 μs
1998 August 16 12:54:00	A	41.469838 s	±	2.0 μs	−0.61 μs
1998 August 16 13:20:00	G	−582341.0 Hz	±	1.5 Hz	0.07 Hz
1998 August 17 11:53:00	A	47.3587963 s	±	2.0 μs	0.99 μs

Transmitter frequency was 8510 MHz for Goldstone (G) or 2380 MHz for Arecibo (A). Astrometry corresponds to echoes from 1998 ML14's center of mass. The reference point for Goldstone is the intersection of the azimuth and elevation axes of the 70 m antenna, DSS-14. The reference point for Arecibo is the 305 m antenna's center of curvature. Residuals are with respect to OSOD Solution 55 (Table 4). The range equivalent of 1 μs is 150 m and the radial velocity equivalents of 1 Hz are 18 mm s^{-1} at 8510 MHz and 63 mm s^{-1} at 2380 MHz.

TABLE 4. Orbit.

Epoch	2451204.5 = 1999 January 26.0 (TDT)	
Eccentricity (e)	0.6167486518	± 0.0000001557
Perihelion distance (q)	0.9257756359 AU	± 0.0000000331 AU
Perihelion passage (T_p)	2451066.8482294103 days (1998 September 10.34823)	± 0.0000060575 days
Long. asc. node (Ω)	339.3870233371°	± 0.0000375813°
Arg. of perihelion (ω)	19.3196258550°	± 0.0000375610°
Inclination	2.4708720689°	± 0.0000041873°
Semimajor axis	2.4155835072 AU	± 0.0000009984 AU
Period	1371.29695126 days (3.75434065292679 years)	+ 0.00085021 days
Mean anomaly	36.1370579630°	± 0.0000223904°

1998 ML14's heliocentric orbital elements (OSOD solution #55) and formal 1σ uncertainties, estimated using our delay-Doppler radar astrometry (Table 3) and currently available optical astrometry (234 optical measurements from 1998 June 24 to 1999 January 24). The mean ± r.m.s. post-fit radar residuals are time delay, 1.09 ± 3.84 μs, and Doppler frequency, 0.65 ± 0.94 Hz. The mean r.m.s. post-fit optical residuals are RA, −0.18 ± 0.73", and declination, −0.03 ± 0.47". Elements are in the coordinate frame of the JPL planetary ephemeris DE-405 (ICRF93/J2000, a quasar-based radio frame, generally within 0.01 arcseconds of the optical FK5/J2000 frame). Angular orbital elements are referred to the ecliptic and mean equinox of J2000.

from a solution (OSOD-55) incorporating all available radar and optical astrometry from 1998 June 24 to 1999 January 24. Distance and radial-velocity equivalents of the r.m.s. delay/Doppler residuals are 0.6 km and 1.7 cm s^{-1}.

How much does radar astrometry improve our knowledge of 1998 ML14's orbit? As shown in Table 5, the 3σ plane-of-sky (POS) uncertainty in 2013 August, during the asteroid's next optically favorable apparition, will be only a few arcminutes with the radar + optical orbit. With a brightness of 15 mag, it should be recovered easily. Without any radar data, the POS uncertainty would be more than 1°. The range uncertainty at the 22-lunar distance (LD) close approach in 2013 is four Earth radii (0.068 LD) for the radar + optical orbit, but 34 Earth radii (0.58 LD) for the optical-only orbit.

Table 6 lists close approaches of 1998 ML14 to inner planets based on the radar + optical orbit solution OSOD-55. Uncertainties increase away from the time interval spanned by astrometry, and we have cut off forward and backward integrations when the 3σ uncertainty in the epoch of closest approach reaches 10 days (14 400 min). The resulting table of useful predictions spans 1183 years, from A.D. 1100 to A.D. 2283. (For an orbit solution lacking radar astrometry, but otherwise having the same optical data, the same criterion would limit

TABLE 5. Prospects for recovering 1998 ML14.

Date	3σ Uncertainties R.A. (arcsec)	Dec. (arcsec)	Doppler (Hz)	Delay (μs)	Dist. (AU)	S-O-E	V (mag)
Radar + Optical Orbit (#55)							
2013 August 03	1.45×10^2	9.61×10^1	2.5×10^2	3.2×10^5	0.136	53°	15.4
2013 August 06	1.04×10^2	1.09×10^2	2.2×10^2	3.4×10^5	0.120	59°	15.3
2013 August 09	3.64×10^1	1.16×10^2	1.7×10^2	3.5×10^5	0.106	67°	15.2
2013 August 12	7.23×10^1	1.10×10^2	1.1×10^2	3.5×10^5	0.092	76°	15.1
2013 August 15	2.45×10^2	7.18×10^1	2.2×10^1	3.5×10^5	0.079	87°	15.2
2013 August 18	5.03×10^2	3.25×10^1	9.6×10^1	3.2×10^5	0.068	101°	15.5
2013 August 21	8.30×10^2	2.30×10^2	2.4×10^2	2.7×10^5	0.060	119°	16.2
2013 August 24	1.11×10^3	4.59×10^2	4.0×10^2	1.7×10^5	0.056	140°	18.1
2013 August 27	1.19×10^3	5.53×10^2	5.1×10^2	5.0×10^4	0.058	162°	23.0
Optical-Only Orbit							
2013 August 03	4.50×10^3	2.90×10^3	6.4×10^3	7.9×10^6	0.120	51°	15.1
2013 August 06	3.31×10^3	3.49×10^3	5.5×10^3	8.2×10^6	0.104	59°	14.9
2013 August 09	1.08×10^3	3.99×10^3	4.3×10^3	8.5×10^6	0.089	67°	14.8
2013 August 12	2.98×10^3	3.97×10^3	2.4×10^3	8.6×10^6	0.075	78°	14.8
2013 August 15	1.00×10^4	2.30×10^3	3.8×10^2	8.3×10^6	0.063	92°	14.9
2013 August 18	2.05×10^4	2.88×10^3	4.2×10^3	7.2×10^6	0.053	110°	15.4
2013 August 21	3.07×10^4	1.10×10^4	8.7×10^3	4.8×10^6	0.049	134°	17.1
2013 August 24	3.36×10^4	1.53×10^4	1.2×10^4	1.5×10^6	0.051	159°	21.5
2013 August 27	2.92×10^4	1.30×10^4	1.3×10^4	1.7×10^6	0.059	176°	42.2

Geocentric ephemerides relevant to recovery of 1998 ML14 in 2013 are shown for radar + optical and optical-only orbit solutions. 3σ uncertainties are given for right ascension (R.A.), declination (Dec.), echo frequency at Goldstone's current transmitter frequency (8560 MHz), and echo time delay. S-O-E is the Sun-Object-Earth angle (the solar phase angle) and V is the visual magnitude.

the useful close-approach prediction interval to the 409 years spanning 1874–2283.) The 1998 apparition was 1998 ML14's closest approach to Earth since at least 1100 and until its 2.4-lunar distance approach in 2283. Orbit uncertainties beyond that date are substantially increased by that event.

DELAY-DOPPLER SIGNATURE AND BASIC RADAR PROPERTIES

Figures 2, 3 and 4 show samples of our cw spectra and delay-Doppler images. The echoes reveal an object with a delay depth consistently within about 15% of 3.5 μs (525 m in range) and an echo bandwidth similarly close to 6.5 Hz at Goldstone's transmitter frequency of 8510 MHz (1.8 Hz at Arecibo's transmitter frequency of 2380 MHz). With the 15-h spin period (Hicks and Weissman, 1998), the echo bandwidth yields the constraint

$$D = (0.97/\cos\delta) \pm 15\% \quad (1)$$

where D is the asteroid's average pole-on breadth in kilometers and δ is the asteroid-centered declination of the radar (*i.e.*, the subradar latitude). The images show a nearly parabolic leading edge of constant size and shape (the classic radar signature of a spherical target) except for a prominent bump and indentation on one side of the asteroid and some less prominent structure elsewhere.

Using the Goldstone cw spectra (probably the most reliably calibrated of any of our data, in part because of uncertainties in the gain of the newly upgraded Arecibo antenna), we obtain an average OC radar cross section, $\sigma_{OC} = 0.095$ km^2 ± 25%, and an average circular polarization ratio, SC/OC = 0.30 ± 0.03. The cross section gives an OC radar albedo of

$$\hat{\sigma}_{OC} = \sigma_{OC}/A_{proj} \quad (2)$$

where A_{proj} is the asteroid's projected area. For a 1 km diameter sphere, $\hat{\sigma}_{OC} = 0.12$. That value is in the lower half of the distribution of values estimated for S-class near-Earth asteroids (NEAs). The SC/OC value is typical of NEAs (mean and r.m.s. dispersion about 0.35 ± 0.25) and is close to values estimated for Apollo, Castalia, Toutatis, and Eros. With the equation (Bowell *et al.*, 1989)

$$\log p_v = 6.259 - 2\log D - 0.4H \quad (3)$$

relating the visual albedo p_v to 1998 ML14's absolute magnitude (currently estimated as $H = 17.5$) and with $D = 1$ km, we obtain $p_v = 0.17$, a typical value for S-class objects. Thus 1998 ML14's disc-integrated radar and optical properties are consistent.

TABLE 6. Close planetary approaches of 1998 ML14.

Date			Body	Close-approach distance Nominal (AU)	Minimum (AU)	Maximum (AU)	V_{rel} (km/s)	ΔT (min)	NSIGS
1100	October	9.9	Earth	0.0718	0.0427	0.1025	12.8	5584	2.10×10^5
1164	August	11.6	Earth	0.0637	0.0586	0.0702	9.9	7938	1.43×10^6
1175	October	1.2	Mars	0.0788	0.0753	0.0883	12.3	2840	3.22×10^5
1337	September	30.5	Earth	0.0414	0.0398	0.0431	10.4	1182	3.37×10^5
1420	April	9.0	Mars	0.0648	0.0646	0.0653	12.8	456	2.92×10^5
1435	April	26.7	Mars	0.0772	0.0759	0.0786	12.5	328	2.98×10^5
1439	January	25.8	Mars	0.0665	0.0663	0.0668	13.3	265	2.90×10^5
1442	October	29.5	Mars	0.0707	0.0699	0.0715	13.6	228	2.87×10^5
1480	June	18.2	Mars	0.0630	0.0627	0.0632	12.6	145	3.03×10^5
1480	September	27.3	Earth	0.0544	0.0539	0.0550	10.0	468	4.39×10^5
1533	February	14.4	Mars	0.0620	0.0614	0.0629	12.9	431	2.94×10^5
1536	November	16.6	Mars	0.0644	0.0633	0.0656	13.4	413	2.92×10^5
1555	September	14.1	Mars	0.0566	0.0563	0.0570	12.9	310	2.81×10^5
1559	June	23.7	Mars	0.0756	0.0740	0.0773	12.0	317	2.87×10^5
1559	October	5.7	Earth	0.0458	0.0446	0.0470	10.2	874	3.60×10^5
1589	July	21.3	Mars	0.0605	0.0600	0.0610	12.8	181	2.86×10^5
1683	July	29.3	Earth	0.0350	0.0348	0.0352	12.4	96	6.84×10^5
1698	July	28.2	Earth	0.0587	0.0577	0.0597	12.8	203	6.34×10^5
1713	September	7.0	Earth	0.0777	0.0777	0.0777	9.8	38	9.34×10^5
1844	September	20.4	Earth	0.0791	0.0791	0.0791	9.8	53	1.50×10^5
1874	November	2.6	Earth	0.0563	0.0556	0.0570	13.2	149	2.84×10^5
1998	**August**	**10.9**	**Earth**	**0.0181**	**0.0181**	**0.0181**	**11.6**	**0**	**8.71×10^5**
2013	August	24.4	Earth	0.0562	0.0560	0.0563	10.3	90	7.24×10^5
2088	November	23.2	Mars	0.0785	0.0780	0.0789	14.4	53	1.38×10^5
2092	August	17.3	Mars	0.0574	0.0569	0.0579	12.4	63	1.42×10^5
2114	November	4.2	Earth	0.0375	0.0374	0.0377	12.3	79	2.90×10^5
2129	November	7.4	Earth	0.0634	0.0621	0.0647	13.1	249	2.74×10^5
2204	August	25.4	Mars	0.0606	0.0592	0.0621	12.1	175	1.24×10^5
2238	October	29.2	Earth	0.0501	0.0501	0.0501	10.8	2	2.48×10^5
2246	January	2.0	Mars	0.0416	0.0412	0.0420	14.0	47	1.11×10^5
2253	August	31.3	Earth	0.0758	0.0753	0.0763	10.4	311	3.06×10^5
2268	August	7.4	Earth	0.0598	0.0589	0.0607	13.6	140	2.96×10^5
2283	August	17.3	Earth	0.0082	0.0070	0.0094	11.7	309	0.86×10^5

Planetary approaches within 0.08 AU are listed along with the nominal, 3σ minimum and 3σ maximum distances. V_{rel} is the relative velocity at the nominal close approach, ΔT is the 3σ uncertainty in the epoch of close approach, and NSIGS is the number of standard deviations required for the uncertainty ellipse to intersect the close-approach body.

SHAPE MODEL

Using the same approach applied to other asteroid radar imaging data sets (*e.g.*, Hudson and Ostro, 1995), we modeled the shape of 1998 ML14 as a 1022-sided polyhedron whose elements' average area is $(58\ \mathrm{m})^2$. The radar observations, which covered a sky arc of only 33°, yield a bandwidth trajectory (Hudson *et al.*, 2000) that establishes that our view of 1998 ML14 was at least several tens of degrees from pole-on, but are inadequate to constrain the pole direction further. We experimented with inclusion of optical lightcurves (Hicks and Weissman, pers. comm.) obtained with the asteroid near (RA, dec.) = (292°, −31°), ~145° from the radar-observed arc. Those data preclude a pole direction within a few tens of degrees of that direction, but are inadequate to produce tighter pole constraints. Our modeling indicates that the rotation period is within 0.15 h of 14.83 h.

Figure 5 shows selected Goldstone and Arecibo images and images generated using the model, along with corresponding POS views of the model, and Fig. 6 shows views of the model along its principal axes. The model's equivalent spherical diameter is within 5% of 1.0 km, its moment-of-inertia ratios are within 5% of 0.99 and 0.94, and its radar scattering law is approximately Lambertian. The shape model reinforces our inferences from visual inspection of the images: 1998 ML14 is a 1 km diameter spheroid with prominent topography on one

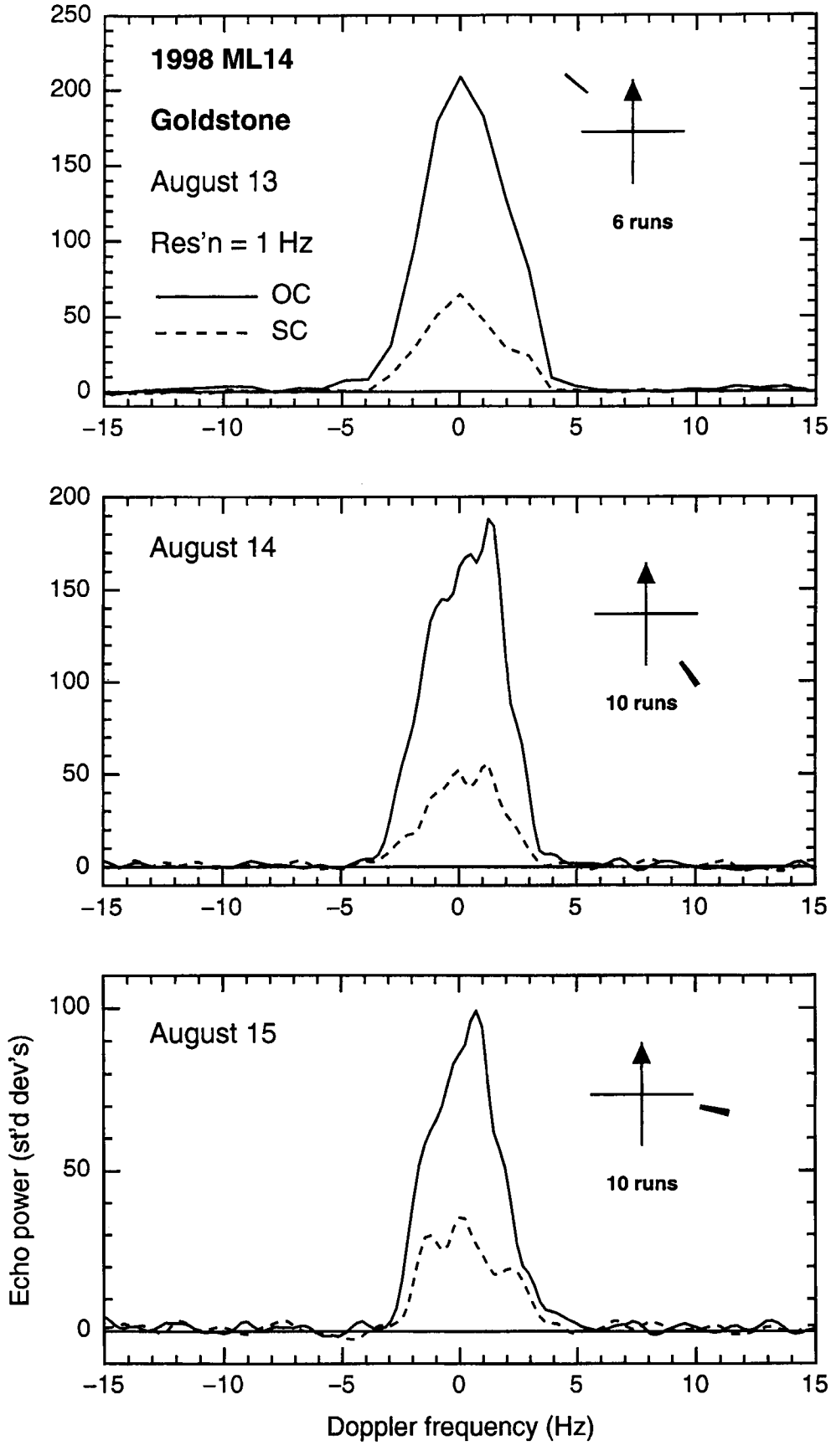

FIG. 2. Goldstone cw echo spectra. Insets indicate relative phase coverage as in Fig. 1.

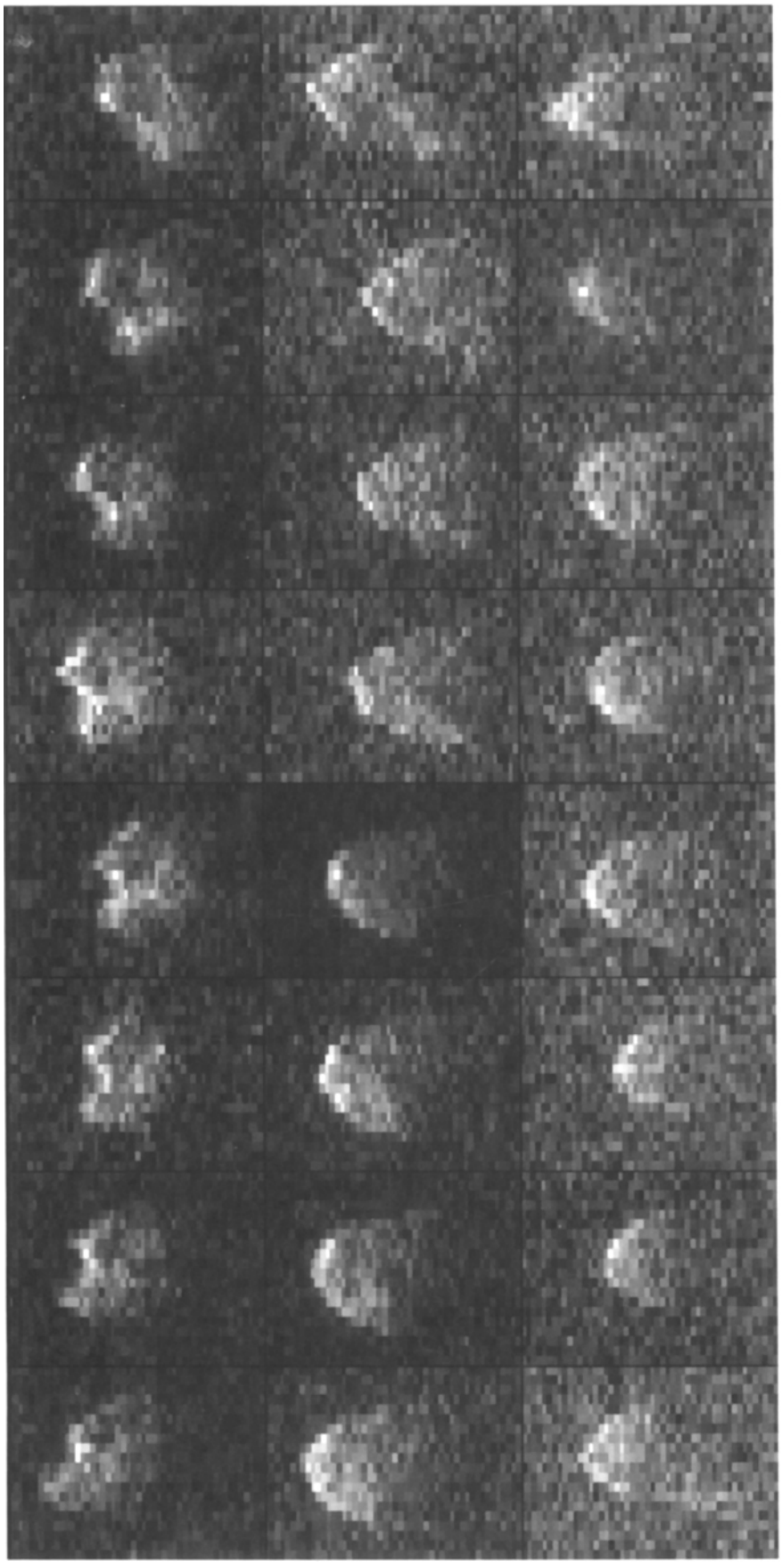

FIG. 3. Summed subsets of Goldstone 0.125 μs × 0.5 Hz images (Table 2). Time increases from left to right and from top to bottom. Range increases from top to bottom, and Doppler frequency increases from left to right, so the rotation is counterclockwise. Each frame shows the same range and Doppler extents. In the top row (August 13), from left to right, the first four frames are from file 22508 and the last four frames are from file 22509. In the middle row (August 14 and 15), the first four frames are from file 22607; the next three are sums of files 22611, 22612, and 22613; the last is from 22703. In the bottom row (August 15 and 16), the first frame is from 22703, the second and third are from 22704, the fourth is a sum of 22707, the fifth and sixth are from 22709, the seventh is from 22804, and the eighth is from 22805. Each frame in the top two rows spans 5° of rotation except for the last two frames in the middle row, which span 2° and 9°. The frames in the thrid row span, from left to right, 9°, 9°, 9°, 12°, 14°, 14°, 20° and 34°.

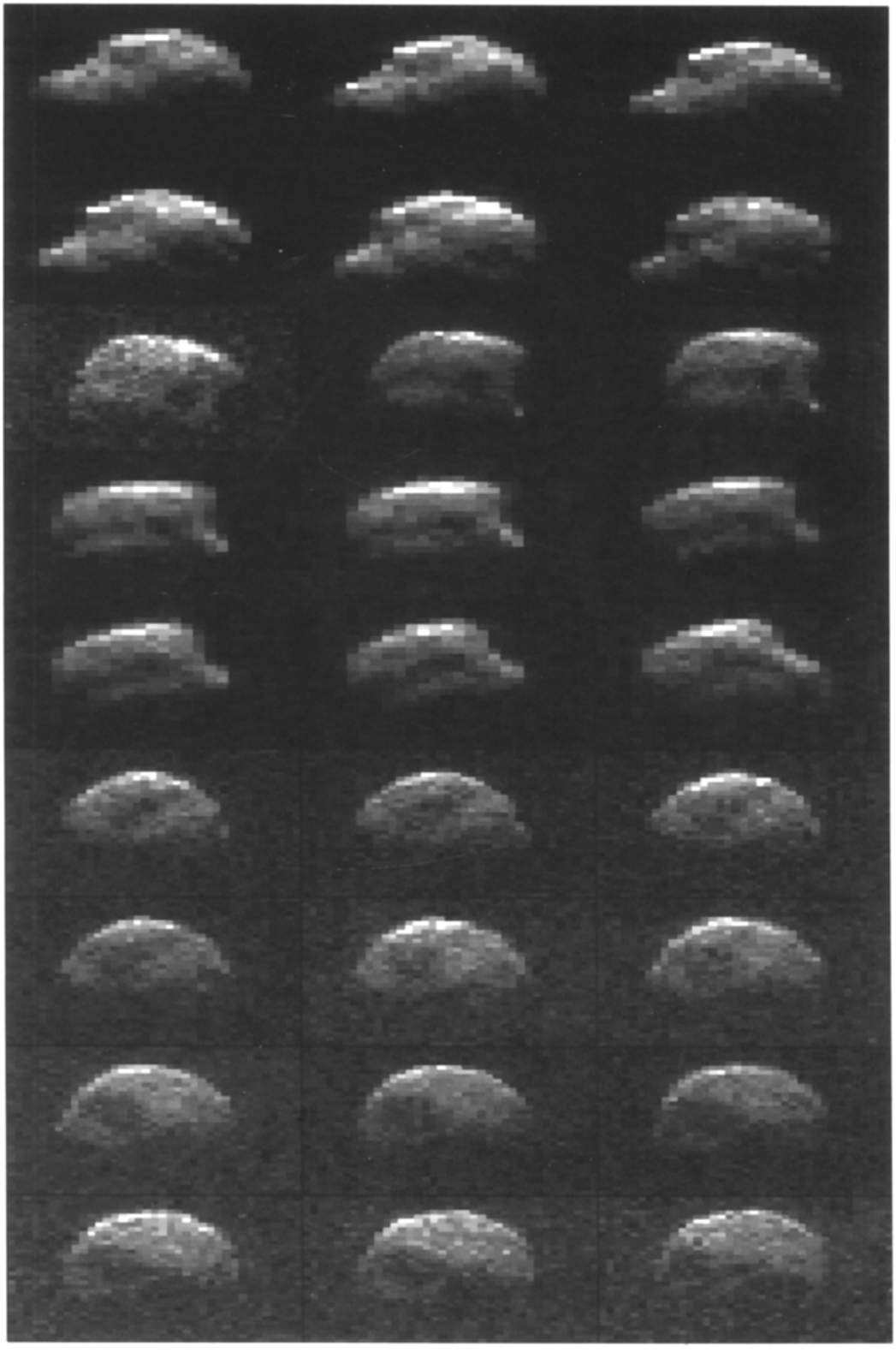

FIG. 4. Summed subsets of Arecibo images (Table 2). Each frame is an integration over ~5° of rotation. Time increases from left to right and from top to bottom. Range increases from top to bottom, and Doppler frequency increases from left to right, so the object's rotation is counterclockwise. Each frame occupies nearly the same range and Doppler extents. The top two rows show 0.3 μs × 0.1 Hz images from August 15, the third shows 0.2 μs × 0.07 Hz images from August 16, the fourth and fifth show 0.3 μs × 0.01 Hz images from August 16, and the bottom four show 0.2 μs × 0.07 Hz images from August 17.

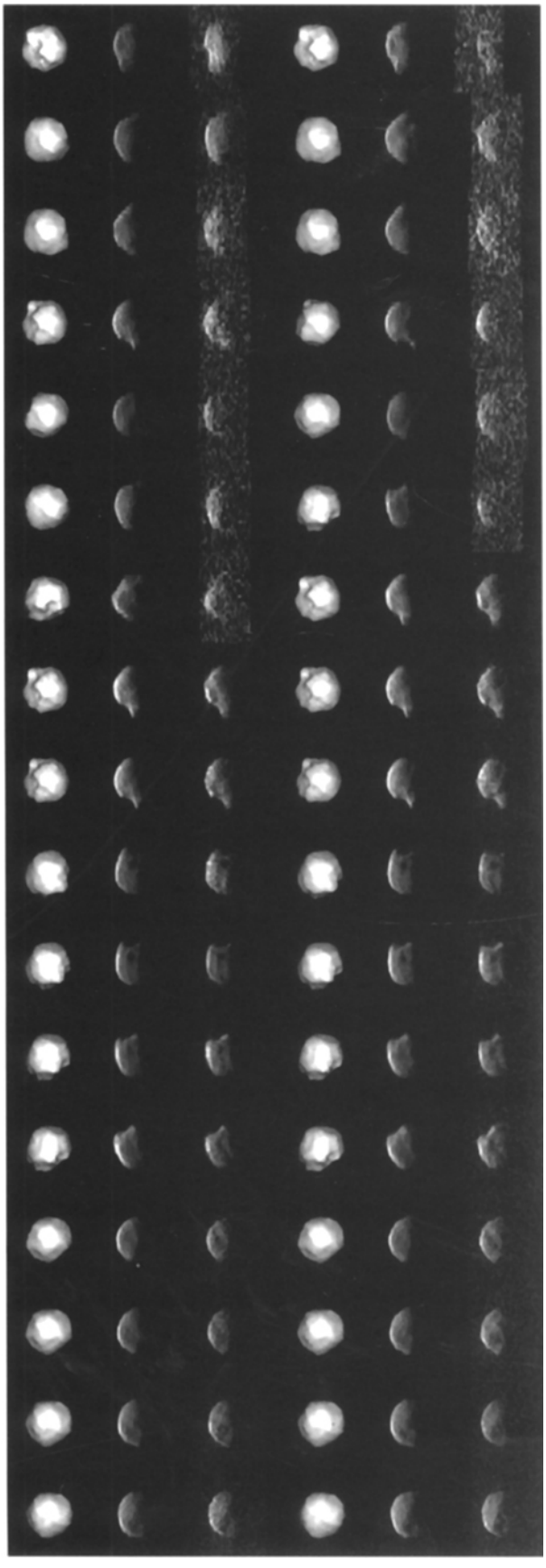

FIG. 5. 1998 ML14 shape model. Selected Goldstone and Arecibo images, the corresponding images predicted by the shape model, and the corresponding plane-of-sky views of the shape model are shown using identical linear scales.

side and subdued topography on the other. The very prominent indentation looks more like a rut or a gouge than a crater.

DYNAMICAL ENVIRONMENT

Let us explore the asteroid's dynamical environment under the assumption that the shape model has a uniform density of 2.5 g cm^{-3}, consistent with its spectral type and with measurements of the internal density distribution of the S-class object 433 Eros by NEAR- Shoemaker (Yeomans *et al.*, 2000). Our calculations, which follow Scheeres *et al.* (1996), indicate that the local acceleration normal to the surface ranges from 0.24 to 0.35 mm s^{-2} and averages 0.32 mm s^{-2}, with the contribution from centrifugal accelerations being no more than 3%. Thus, unlike asteroids with more rapid spin rates, 1998 ML14's surface dynamics are dominated by gravitational processes alone. The escape speed at the model asteroid's surface ranges from 0.53 to 0.65 m s^{-1} and averages 0.59 m s^{-1}.

In Fig. 6, the model's surface is color-coded for gravitational slope S_{grav}, that is, the acute angle that a plumb line would make with the local surface normal. S_{grav} averages 14°, exceeds 10° over 66% of the surface, exceeds 15° over 41% of the surface, and exceeds 30° over only 4% of the surface. (A similar paucity of gravitational slopes larger than 30° has been found for Eros; Zuber *et al.*, 2000.) The largest values of S_{grav}, ~43° on the inside slopes of negative-relief features, are at the large end of the distribution for the angle of repose for loose piles of particles, so it is possible that those regions are relatively regolith-free, with some exposure of bedrock.

Our model predicts that 1998 ML14's near-surface orbital environment is similar to that for a planetary body with a spheroidal gravitational field. It can stably support orbital motions at relatively low altitudes and (given its heliocentric orbit; Hamilton and Burns, 1992) out to 55 asteroid radii. Moreover, it may be possible for impact ejecta to survive in long-lived, stable orbits (Scheeres and Marzari, 2000).

DISCUSSION

Of the asteroids for which spatially resolved radar or optical images are available, the one most similar to 1998 ML14 is 243 Ida's satellite Dactyl, an S-class object whose overall dimensions of about 1.6 × 1.4 × 1.2 km make it the smallest object imaged by spacecraft (Veverka *et al.*, 1996). The radar images of 1998 ML14 and the Galileo images of Dactyl have comparable pixel sizes. However, the latter were taken at solar phase angles between 27° and 96° while our radar images have zero-phase-angle (opposition) illumination and a shadowing geometry radically different from that in conventional optical pictures. Thus Dactyl is readily seen to be a heavily cratered

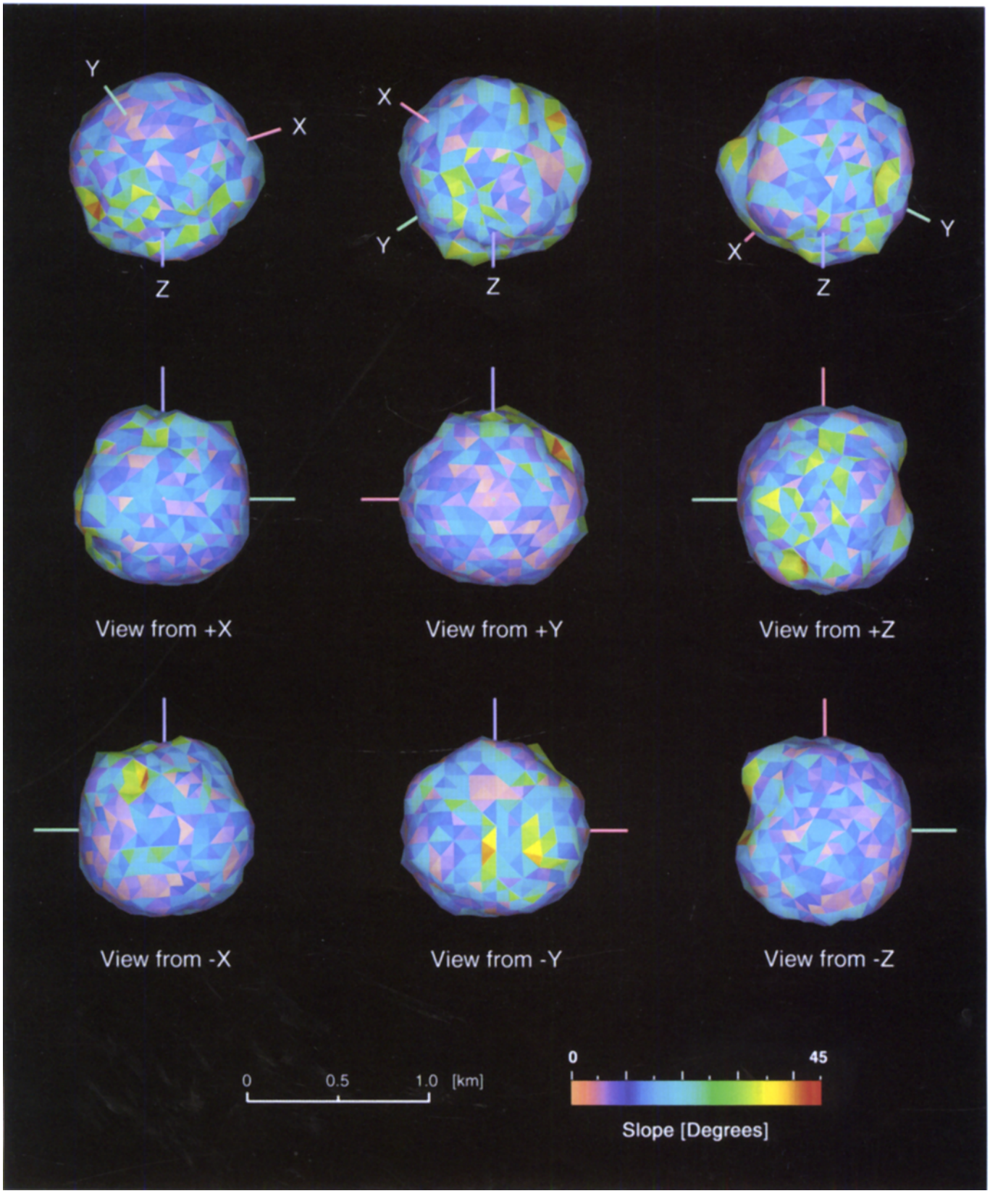

FIG. 6. Views of the 1998 ML14 model, color-coded for gravitational slope S_{grav}. The object rotates about the z axis, which is the principal axis with maximum moment of inertia. The x axis has minimum moment of inertia.

object whereas we cannot be sure that the numerous subtle concavities on 1998 ML14 are impact craters, although that seems likely. On the other hand, each object has a similar degree of limb relief and neither is an angular body.

Our model's pole-on elongation is 1.1 ± 0.1. The 20 other NEAs for which useful radar-derived shape information is available have elongations ranging from 1.2 to 2.5, with a median of 1.4 and a mean and r.m.s. dispersion of 1.6 ± 0.4. 1998 ML14 is among the most spheroidal NEAs in the radar sample.

1998 ML14 and Eros have similar values of SC/OC and hence similar degrees of small-scale roughness. On the other hand, 1998 ML14 is only ~60% as radar bright as Eros and therefore has a somewhat lower near-surface bulk density. If all of 1998 ML14's OC echo were due to reflections from smooth surface elements, then its surface bulk density, calculated using empirical formulas (*e.g.*, Garvin *et al.*, 1985) would not exceed 2.5 g cm^{-3}. Since some of the OC echo surely arises from other kinds of scattering, that value is a safe upper limit for the smooth component of the asteroid's surface.

1998 ML14's combination of modest surface bulk density, mostly shallow gravitational slopes, and spheroidal shape might be taken to suggest that its surface, and possibly much of its interior, might be a regolithic agglomeration of unconsolidated fragmental debris. However, those same characteristics apply to the 30 m object 1998 KY26 (Ostro *et al.*, 1999), whose 11 min rotation indicates a monolithic structure; in any case, there seems to be no easy way to test the validity of this guess. Similarly, we cannot tell whether the topographic relief defined by 1998 ML14's largest protrusions is merely due to impact cratering *per se*, or instead is the surficial manifestation of several-hundred-meter boulders, or some combination of the two.

Acknowledgments–We are grateful to A. Crespo, A. Hine, P. Perillat and the staff of the Arecibo Observatory. We thank S. Suzuki for preparing the cover figure. Part of this research was conducted at the Jet Propulsion Laboratory, California Institute of Technology, under contract with the National Aeronautics and Space Administration (NASA). Work at Washington State University was supported in part by NASA grant NAGW-4636. L. A. M. Benner was supported in part as a Research Associate of the National Research Council. D. J. Scheeres acknowledges support from a grant from the Planetary Geology and Geophysics program in NASA's Office of Space Science. The Arecibo Observatory is part of the National Astronomy and Ionosphere Center, which is operated by the Cornell University under a cooperative agreement with the National Science Foundation and with support from NASA.

Editorial handling: B. Clark

REFERENCES

BOWELL E., HAPKE B., DOMINGUE D., LUMME K., PELTOMIEMI K. AND HARRIS A. W. (1989) Application of photometric models to asteroids. In *Asteroids II* (eds. R. P. Binzel, T. Gehrels and M. S. Matthews), pp. 524–556. Univ. Arizona Press, Tucson, Arizona, USA.

GARVIN J. B., HEAD J. W., PETTENGILL G. H. AND ZISK S. H. (1985) Venus Global radar reflectivity and correlations with elevation. *J. Geophys. Res.* **90**, 6859–6871.

HAMILTON D. P. AND BURNS J. A. (1992) Orbital stability zones about asteroids II. The destabilizing effects of eccentric orbits and of solar radiation. *Icarus* **96**, 43–64.

HICKS M. AND WEISSMAN P. (1998) 1998 ML14. *IAU Circular 6987*. 1 p.

HUDSON R. S. AND OSTRO S. J. (1995) Shape and non-principal-axis spin state of asteroid 4179 Toutatis. *Science* **270**, 84–86.

HUDSON R. S. *ET AL.* (2000) Radar observations and physical modeling of asteroid 6489 Golevka. *Icarus* **148**, 37–51.

OSTRO S. J. *ET AL.* (1999) Radar and optical observations of asteroid 1998 KY26. *Science* **285**, 557–559.

SCHEERES D. J. AND MARZARI F. (2000) Temporary orbital capture of ejecta from comets and asteroids: Application to the Deep Impact experiment. *Astron. Astrophys.* **356**, 747–756.

SCHEERES D. J., OSTRO S. J., HUDSON R. S. AND WERNER R. A. (1996) Orbits close to asteroid 4769 Castalia. *Icarus* **121**, 67–87.

VEVERKA J. *ET AL.* (1996) Dactyl: Galileo observations of Ida's satellite. *Icarus* **120**, 200–211.

YEOMANS D. K. *ET AL.* (2000) Radio science results during the NEAR-Shoemaker spacecraft rendezvous with Eros. *Science* **289**, 2085–2088.

ZUBER M. T. *ET AL.* (2000) The shape of 433 Eros from the NEAR-Shoemaker laser rangefinder. *Science* **289**, 2097–2101.